Supporting Information

Quantitative Determination of Metal Ion Adsorption on Cellulose Nanocrystals Surfaces

Harrison R. Paul[1], Mrinal K. Bera[2], Nicholas Macke[1], Stuart J. Rowan[,1,3,4], and Matthew V. Tirrell[*,1,5]*

[1]Pritzker School of Molecular Engineering, University of Chicago, Chicago, IL 60637, USA

[2]NSF's ChemMatCARS, Pritzker School of Molecular Engineering, University of Chicago, IL 60637, USA
[3]Department of Chemistry, University of Chicago, Chicago, IL 60637, USA

[4]Chemical Science and Engineering Division and Center for Molecular Engineering, Argonne National Laboratory, 9700 S. Cass Ave., Lemont, IL 60434, USA

[5]Materials Science Division and Center for Molecular Engineering, Argonne National Laboratory, 9700 S. Cass Ave., Lemont, IL 60434, USA

Table of Contents:

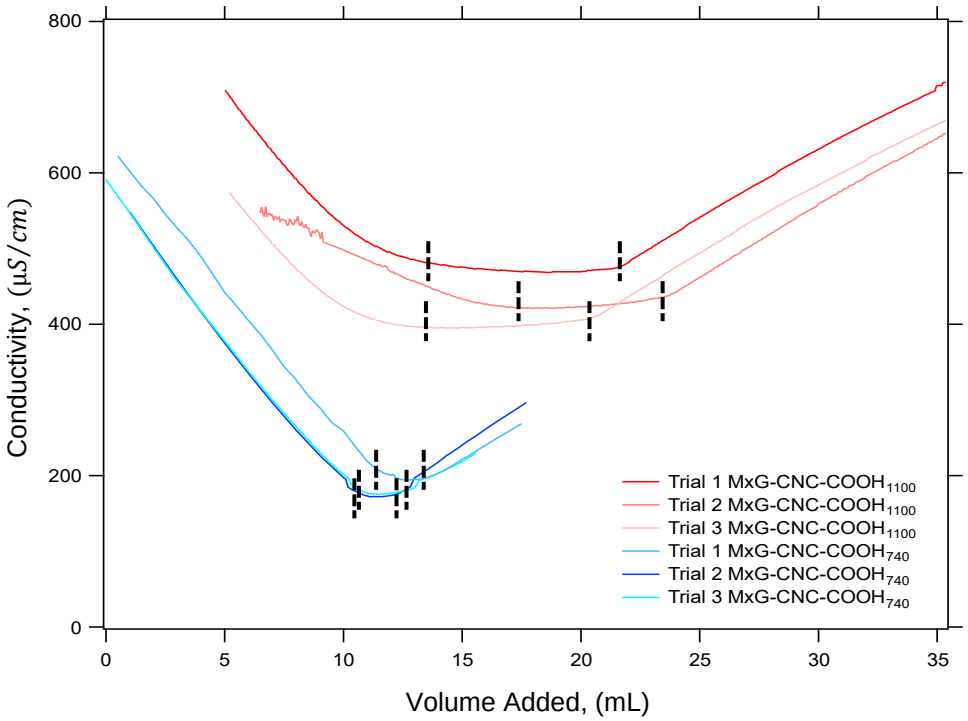

Figure S1. Plot of the Conductivity versus the volume of 0.01 M NaOH added to determine the amount of -COOH (X) present on the *MxG*-CNC-COOH$_X$ surfaces.[1] The amount of -COOH (X) was determined by the length of the weak acid neutralization regime which corresponds to the plateaus in the curves as denoted by the black lines on each curve.

Table S1. Conductivity titration results used to measure the amount of -COOH on the surface of both *MxG*-CNC-COOH samples.

Samples	CNC Mass (mg)	Plateau Volume (mL)	-COOH(X) Concentration ($^{mmol}/_{kg}$)	-COOH Density ($^{groups}/_{nm^2}$)
MxG-CNC-COOH$_{1100}$ 1	68	7.8	1147	1.20
MxG-CNC-COOH$_{1100}$ 2	48	5.9	1229	1.28
MxG-CNC-COOH$_{1100}$ 3	65	6.9	1062	1.11
Average			**1100 ± 100**	**1.2 ± 0.1**
MxG-CNC-COOH$_{740}$ 1	23.5	1.75	742	0.77
MxG-CNC-COOH$_{740}$ 2	25.33	1.73	683	0.71
MxG-CNC-COOH$_{740}$ 3	25.33	2.02	796	0.83
Average			**740 ± 56**	**0.77 ± 0.06**

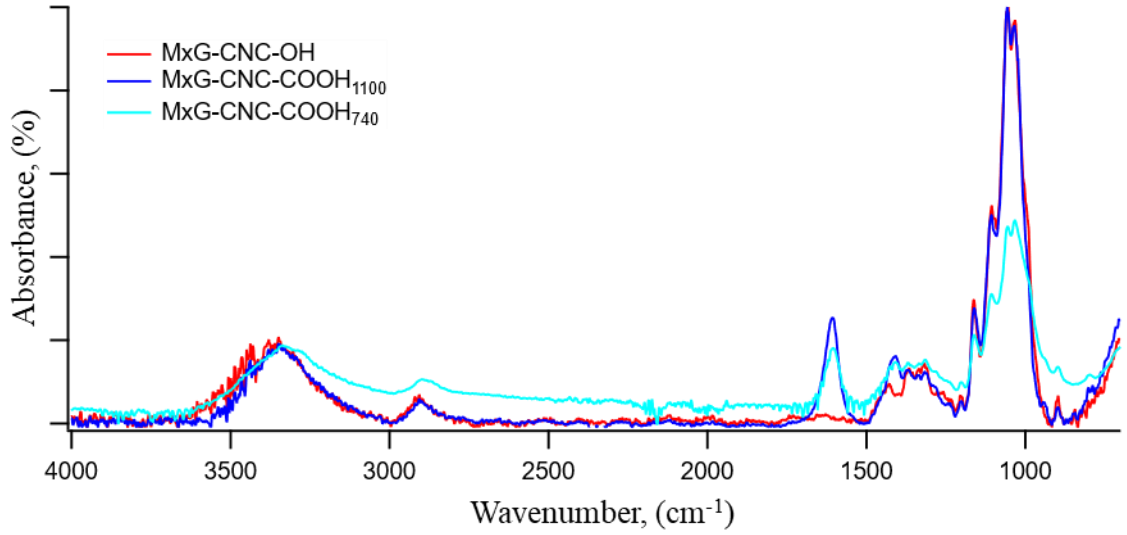

Figure S2. FTIR data showing the emergence of a peak that corresponds to a carbonyl stretch (@ 1600 cm^{-1}) that confirms the functionalization of *MxG*-CNC-OH into *MxG*-CNC-$COOH_X$

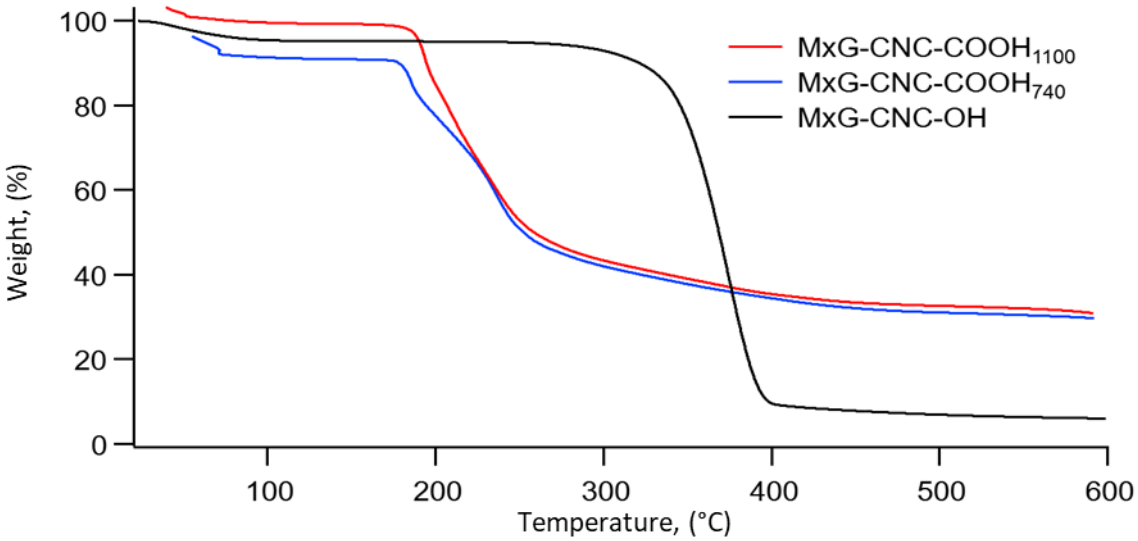

Figure S3. Hi-Res TGA curves for *MxG*-CNC-$COOH_{1100}$ (red), *MxG*-CNC-$COOH_{740}$ (blue), and *MxG*-CNC-OH (black) showing a shift in the degradation pattern and an increase in char yield after successful -COOH functionalization.

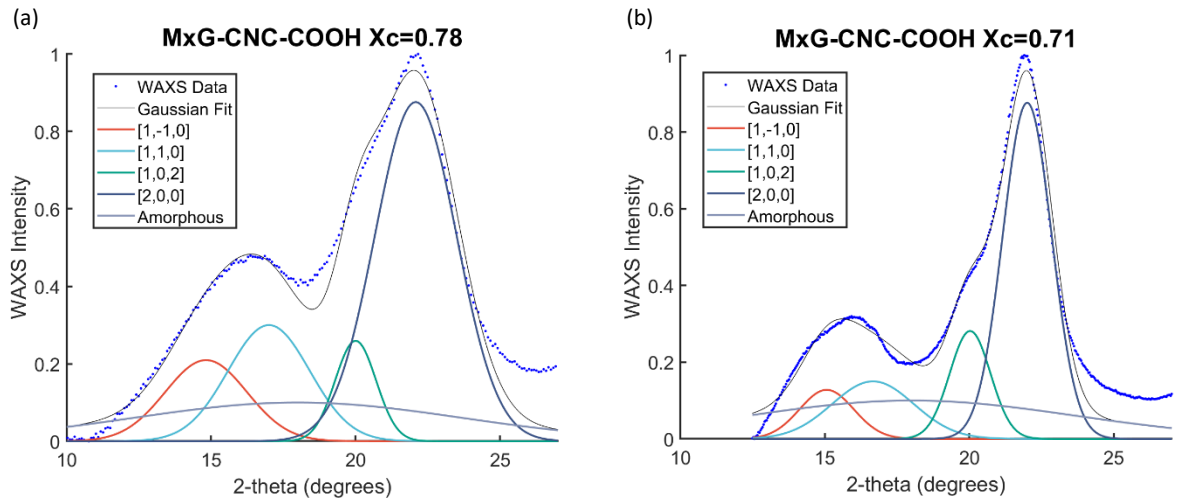

Figure S4. Wide angle X-ray scattering data (blue dots) plotted with Gaussian deconvolution peaks associated with each crystal plane to determine the crystallinity index of the *MxG*-CNC-COOH$_X$ Samples.[1] a) *MxG*-CNC-COOH$_{1100}$ has a crystallinity index of 0.78. b) *MxG*-CNC-COOH$_{740}$ has a crystallinity index of 0.71.

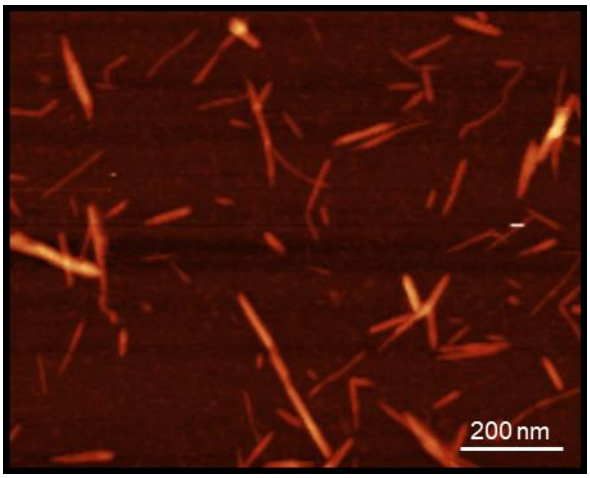

Figure S5. AFM Image of *MxG*-CNC-COOH$_{740}$ on a mica substrate

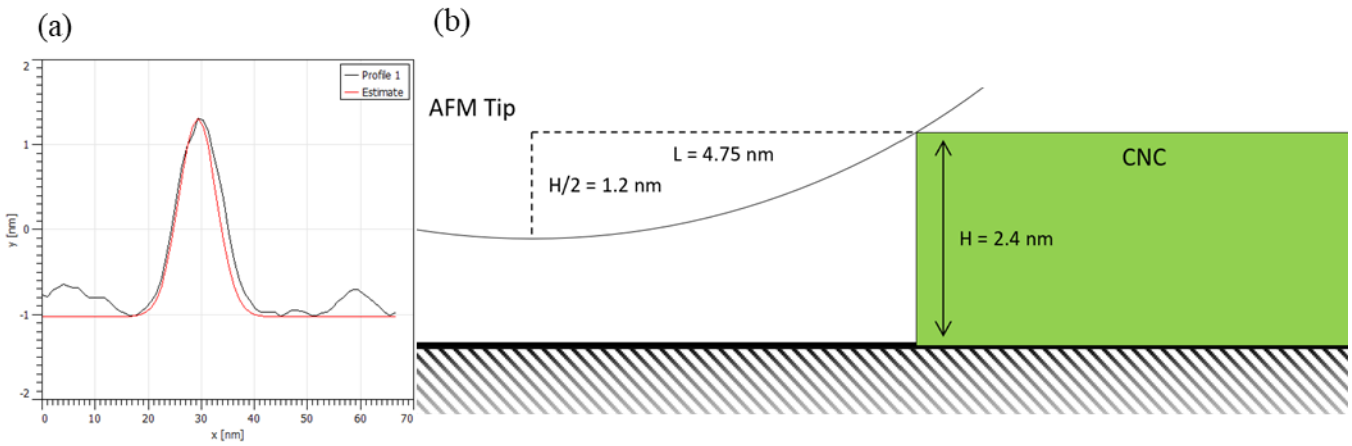

Figure S6. (a) Characteristic AFM height profile of a CNC (black) as well as the gaussian fit used to measure CNC width (red), and (b) schematic of AFM tip broadening as a result of the AFM tip radius (10 nm) being much larger than the CNC width (3.5 nm). This figure illustrates how the measured FWHM is considerably large than the actual CNC dimensions. Dimensions are scaled to match the AFM tip size and CNC height measured in this work.

CNC width measurements were done by fitting AFM height profiles with a Gaussian profile in the Gwyddion software (Figure S6(a)), then taking the full width at half of the peak maximum (FWHM) using the equation $FWHM = \sqrt{2 \ln 2}\, b$, where b is a fit parameter output by Gwyddion. To correct for AFM tip broadening, the AFM tip radius and CNC height can be used to calculate the additional width contributed by tip curvature. With FS-1500 AFM tips from Asylum Research, the tip radius is 10 nm and the height of the *MxG*-CNC-$COOH_{1100}$ measured via AFM is 2.4 nm. Using the trigonometry illustrated in Figure S6(b), the additional width at the half height on one side of the CNC can be calculated to be 4.75 nm using the equation $L = \sqrt{r^2 - d^2}$, where r is the tip radius (10 nm) d is the tip radius minus half the CNC height (8.8 nm) and L is the additional width. Subtracting $2L$ from the measured width of 13 nm results in a corrected MxG-CNC-$COOH_{1100}$ width of 3.5 nm.

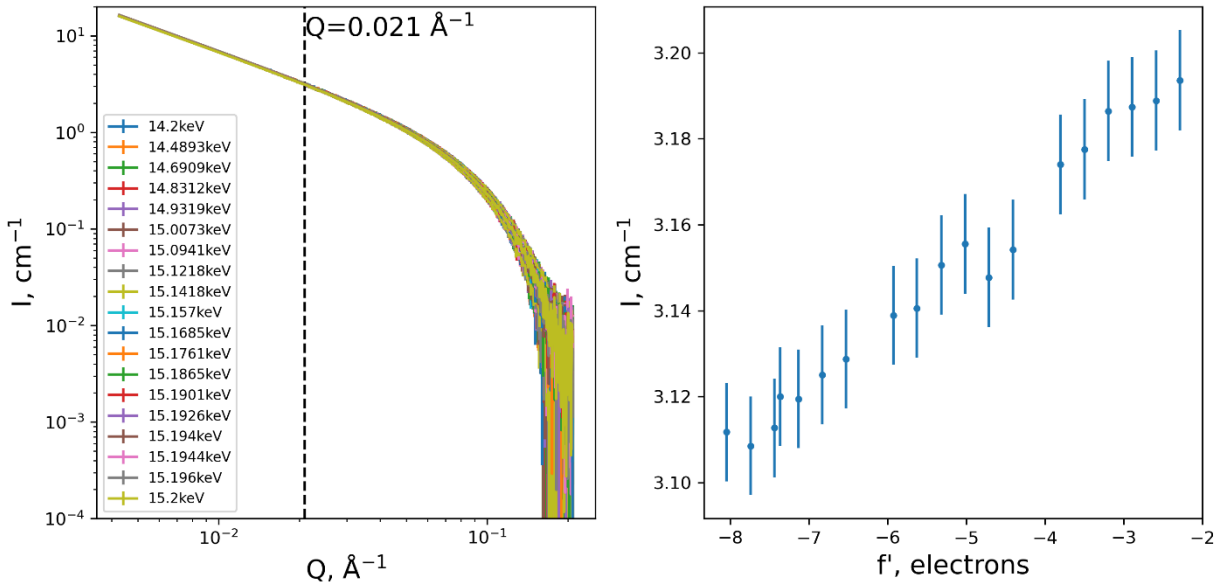

Figure S7. (left) Energy-dependent SAXS patterns simulated with CNCs of dimensions (H=2.4nm, W=3.5nm, L=250.0nm) with Stern layer of Rb^+ ions of thickness 0.332 nm surrounding the nanocrystals (statistical error bars were estimated based on experimental data shown in Figure 1(e)). (right) The energy dependence of SAXS intensity at Q=0.021, as shown with dashed black vertical line in (left).

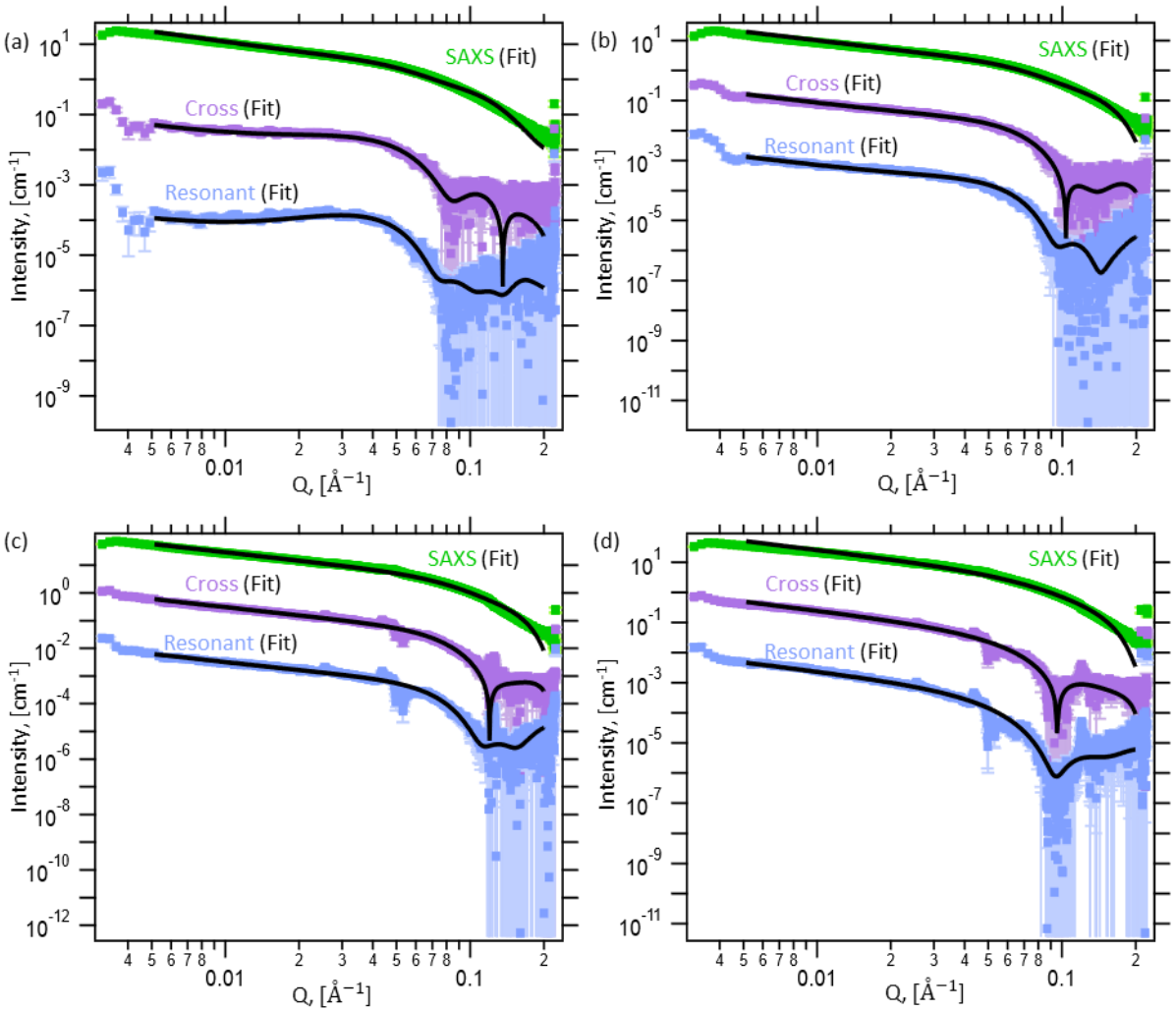

Figure S8. Data from *MxG*-CNC-COOH$_{1100}$ the ASAXS data with the parallelepiped fit. ASAXS data from *MxG*-CNC-COOH$_{1100}$ in (a) 50 mM RbCl solution, (b) 100 mM RbCl solution, (c) 200 mM RbCl solution, and (d) 400 mM RbCl solution

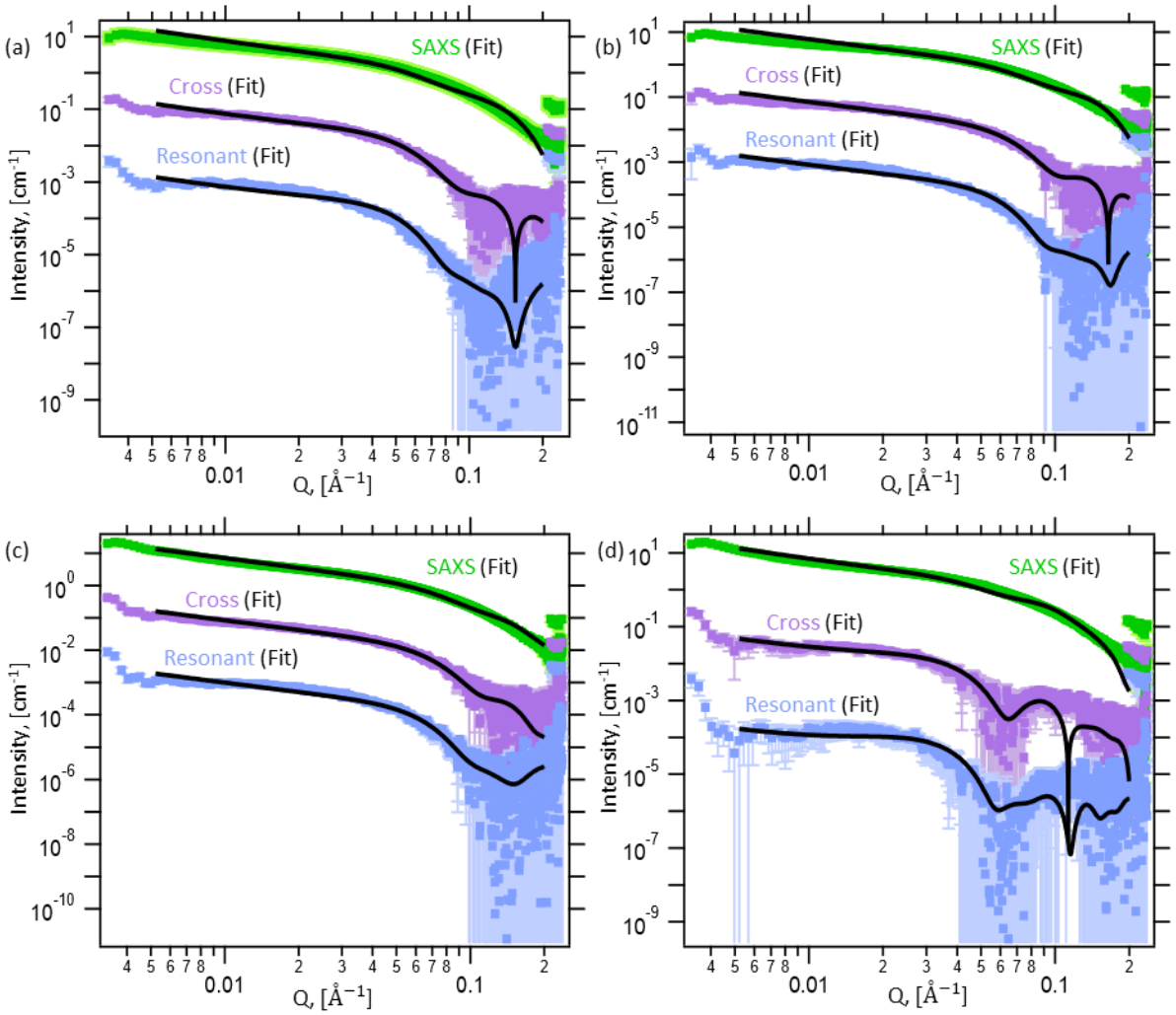

Figure S9. Data from *MxG*-CNC-COOH$_{1100}$ the ASAXS data with the parallelepiped fit. ASAXS data from *MxG*-CNC-COOH$_{1100}$ in (a) 50 mM $SrCl_2$ solution, (b) 100 mM $SrCl_2$ solution, (c) 200 mM $SrCl_2$ solution, and (d) 400 mM $SrCl_2$ solution

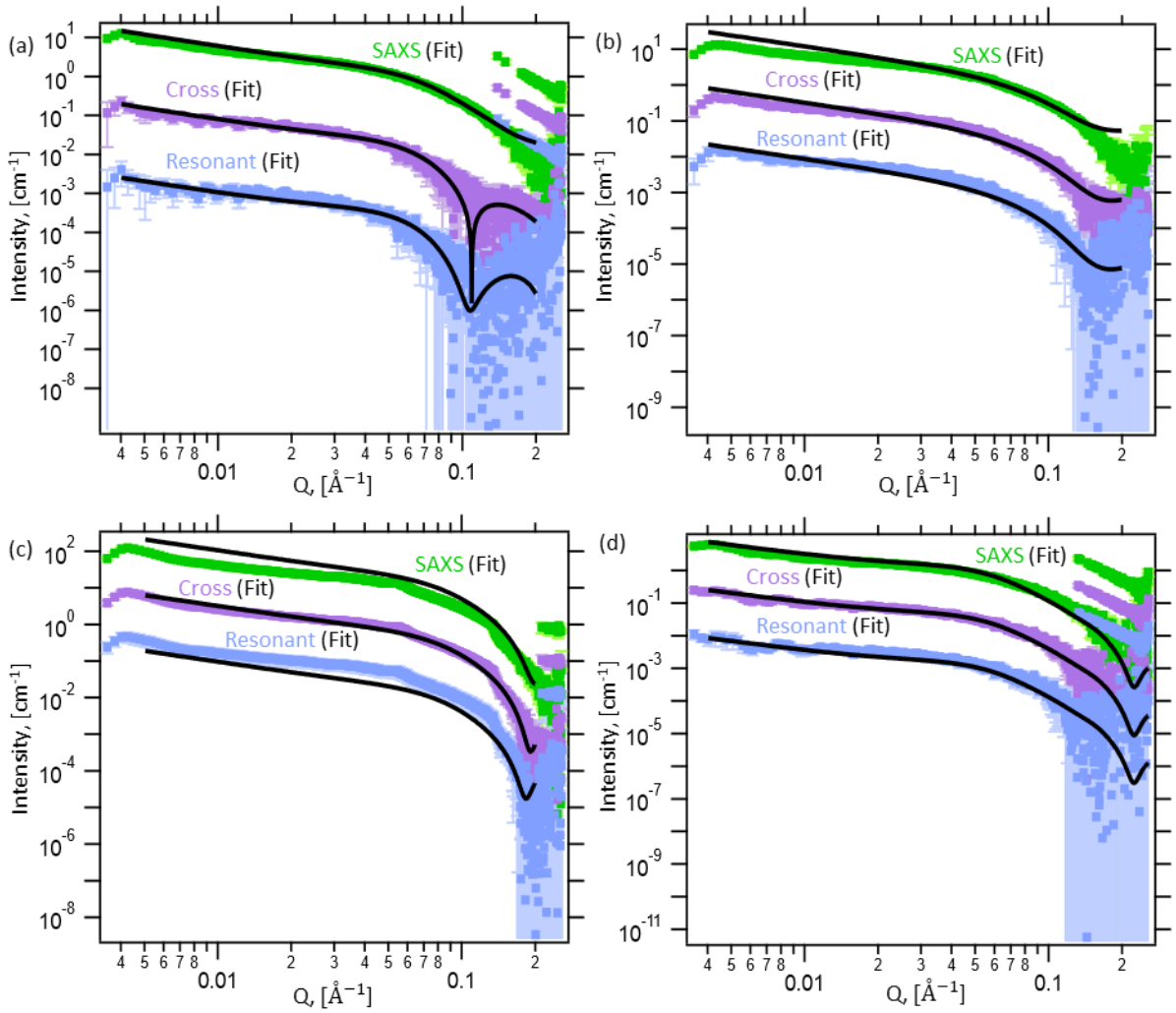

Figure S10. Data from *MxG*-CNC-COOH$_{1100}$ the ASAXS data with the parallelepiped fit. ASAXS data from *MxG*-CNC-COOH$_{1100}$ in (a) 50 mM YCl_3 solution, (b) 100 mM YCl_3 solution, (c) 200 mM YCl_3 solution, and (d) 400 mM YCl_3 solution

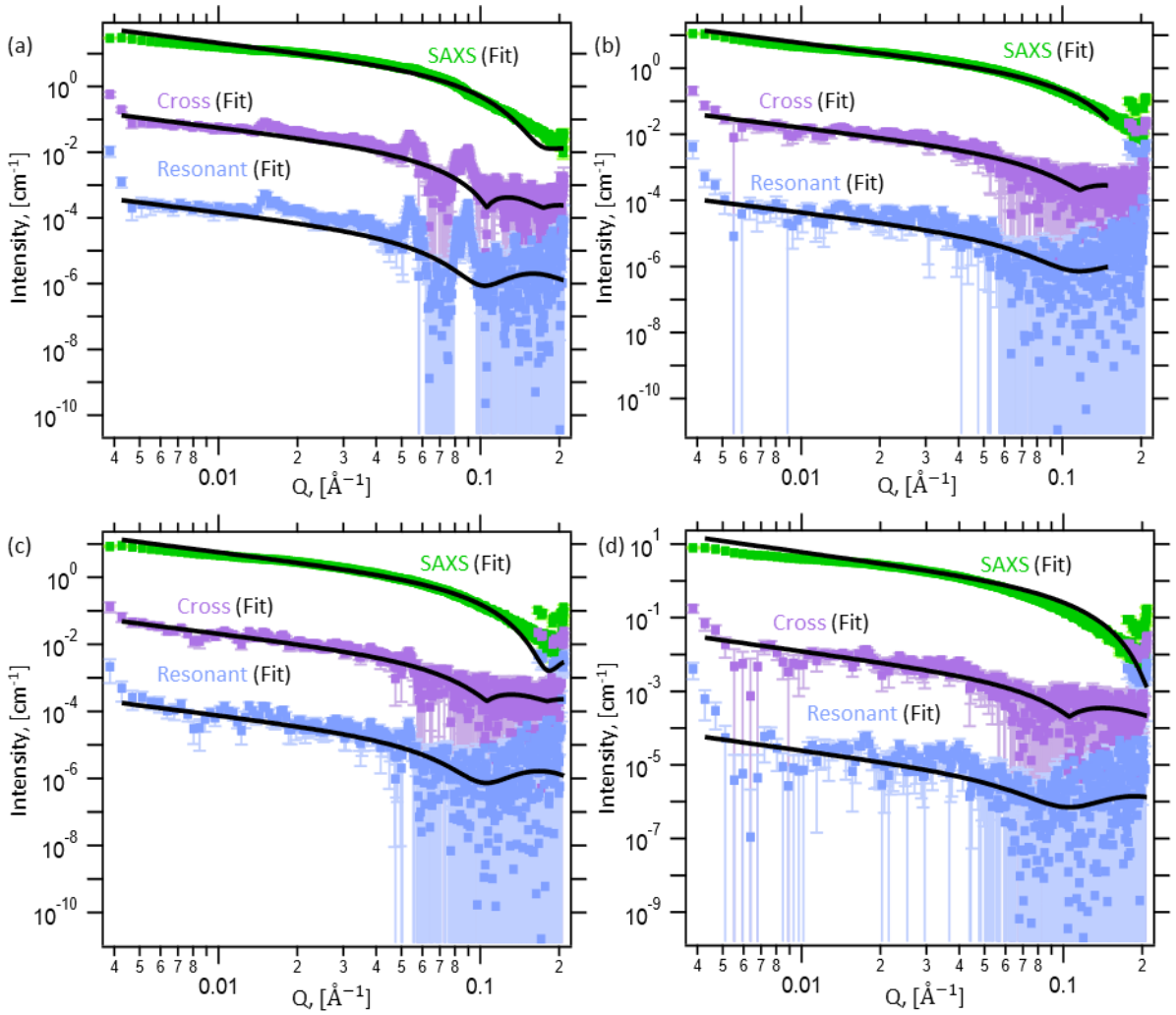

Figure S11. Data from *MxG*-CNC-COOH$_{740}$ the ASAXS data with the parallelepiped fit. ASAXS data from *MxG*-CNC-COOH$_{740}$ in (a) 50 mM RbCl solution, (b) 100 mM RbCl solution, (c) 200 mM RbCl solution, and (d) 400 mM RbCl solution

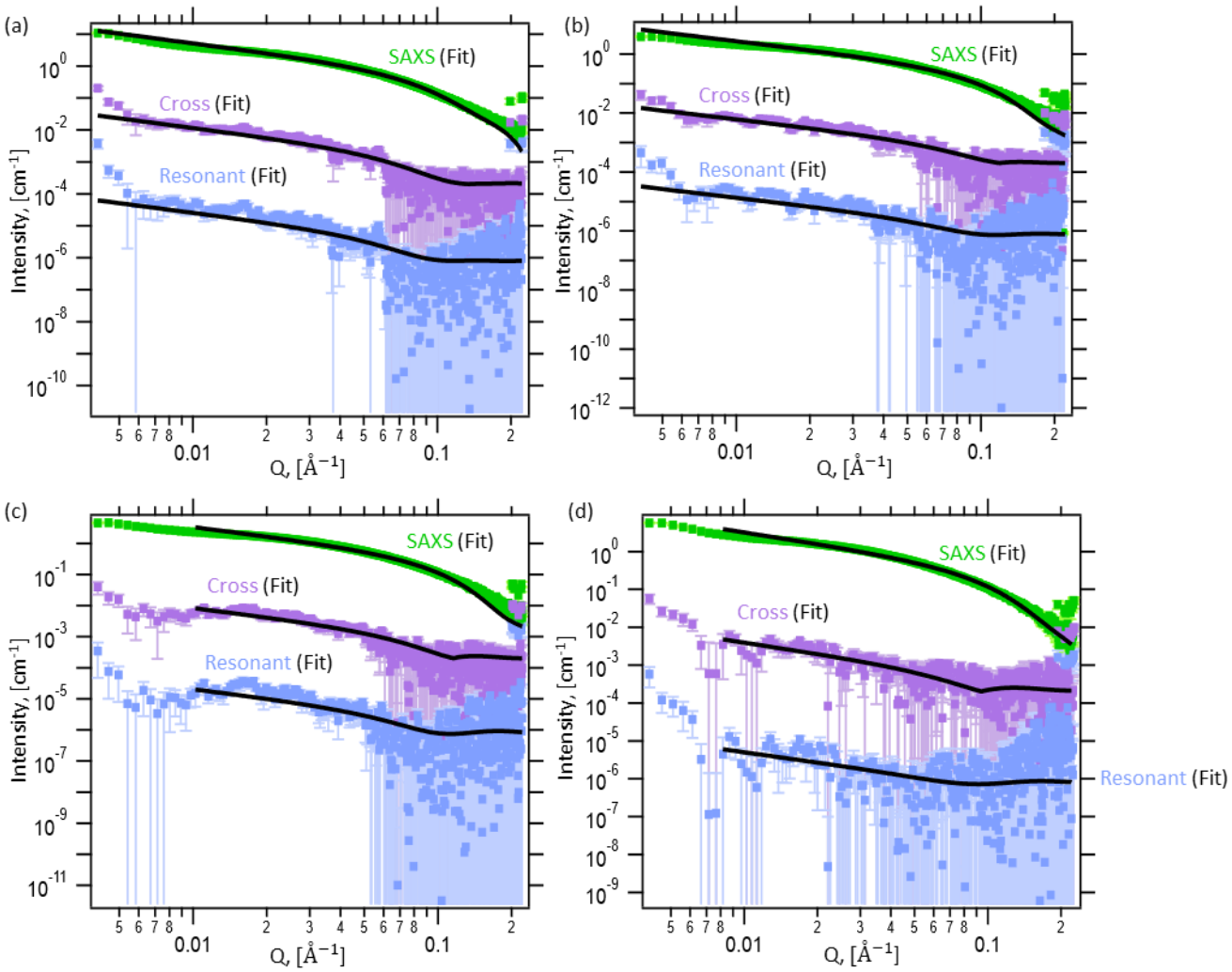

Figure S12. Data from *MxG*-CNC-COOH$_{740}$ the ASAXS data with the parallelepiped fit. ASAXS data from *MxG*-CNC-COOH$_{740}$ in (a) 50 mM $SrCl_2$ solution, (b) 100 mM $SrCl_2$ solution, (c) 200 mM $SrCl_2$ solution, and (d) 400 mM $SrCl_2$ solution

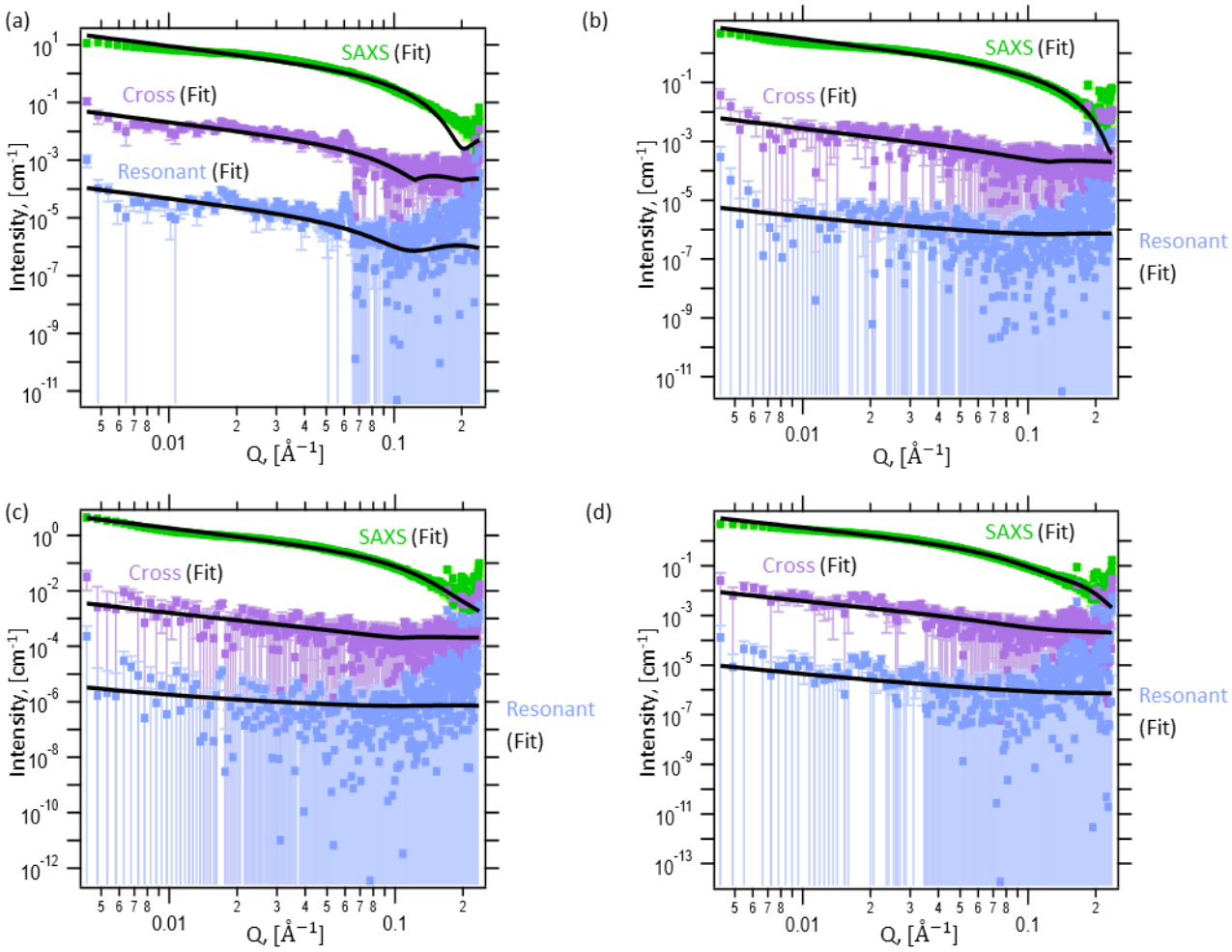

Figure S13. Data from *MxG*-CNC-COOH$_{740}$ the ASAXS data with the parallelepiped fit. ASAXS data from *MxG*-CNC-COOH$_{740}$ in (a) 50 mM YCl_3 solution, (b) 100 mM YCl_3 solution, (c) 200 mM YCl_3 solution, and (d) 400 mM YCl_3 solution

Section S1. Multilayered Parallelepiped Model and functions developed under XModFit

In order to model ion-distribution surrounding parallelepiped CNCs a Multilayered Parallelepiped Model is developed as shown in Figure 1c of the main text. The multilayered parallelepiped is defined by the core's linear dimensions ($L_o \times B_o \times H$) and the shells of different thicknesses (t_i) on top of the core. In the model heights of the shells are kept the same as the core whereas the shell thicknesses can be variable. For analyzing the ASAXS data obtained from CNCs in the present case we only used an one-shell model for the Stern-layer and a two-shell model for the Stern-layer and diffuse layer on top of the CNCs. In general, the heights of the CNCs are much longer than the lengths and breadths and are not accessible in the q-range in the ASAXS data. Hence, for our analysis we kept the heights fixed with the values obtained from AFM. Assuming the CNCs are randomly oriented with respect to the X-Ray beam and randomly spatially distributed (Structure factor, $S(q) = 1$) the intensity from the CNCs can be the form factor of parallelepiped as:[2]

$$I(q) = \frac{N}{V}\left|\sum_{i=0}^{N_L} L_i B_i H(\rho_{e,i} - \rho_{e,i+1}) \int_0^{2\pi}\int_0^{\pi} \mathrm{sinc}^2 A_i \,\mathrm{sinc}^2 B_i \,\mathrm{sinc}^2 C \sin\phi \, d\phi d\psi\right|^2 \quad \text{S1}$$

Where $A_i = qL_i \sin\phi \cos\psi /2$, $B_i = qB_i \sin\phi \cos\psi /2$, and $C = qH \cos\phi /2$ with ϕ and ψ being the polar and azimuthal angles in spherical polar co-ordinates with X-axis being the direction of the beam. The layer corresponding to $i = 0$ represent the core with electron density, $\rho_{e,o}$, and dimensions, (L_o, B_o, H). Whereas, the layer coresponding to the last shell with electron density, $\rho_{e,L}$, and dimensions, $(L_{N_L} = (L_0 + \sum_{j=1}^{J=NL} t_j),\ B_{N_L} = (B_0 + \sum_{j=1}^{J=NL} t_j),\ H)$, resepectively. $i = N_L$+1 represents the bulk medium with electron density, ρ_{es}, in which the parallelepiped is dispersed randomly. In order to incorporate polydispersity of the CNCs, equation S1 can be either integrated over 'Gaussian' or 'Log-Normal' distributions over the lateral core dimensions (L_0, B_0). The energy dependent intensity in equation S1 can be calculated using the energy-dependent electron densities of the multilayers of the parallelepiped calculated from equation S2. Electron density of a layer is calculated from the elemental composition of the layer provided by the molecular formula and the mass density of the layer. All the calculations are implemented in the form of two functions 'Parallelepiped_Uniform' and 'Parallelepiped_Uniform_Edep' in the XModFit package developed by NSF's ChemMatCARS.[3] 'Parallelepiped_Uniform' calculates the SAXS-term, the Cross-term, and the Anomalous-term from the model whereas 'Parallelepiped_Uniform_Edep' calculates energy dependent total SAXS intensity from the parallelepiped model. In the XModfit package the materials for the two functions are defined as 'Multiple fitting parameters' as:

1) If the material is in solid form with known elemental composition the material can be defned by its Chemical Formula (Example: Au, Ag, AgNO3..etc).

2) The moles of the resonant element in the molecular formula will be defined by the parameter 'Rmoles'.

3) If the material is defined as a solution where the material composition will be written in the format of 'Solute:Solvent' where both the 'Solute' and 'Solvent' material described by their respecitve chemical formulas with known elemental compositions (Example: AuCl3:H2O, NaCl:H2O etc)

4) If the resonant element of a material (R) is shared with another element (C), the material should be described as chemical formula as $A_{nA}B_{nB}C_{nC}$*$E_{nE}R$, where (A, B, E) are non-resonant elements with (nA, nB, nE) moles, respectively, and R is the resonant element with 'Rmoles' moles. The number of moles of 'C' in the chemical formula will be (nC-Rmoles).

5) The density of the 'solute' and 'solvent' are provided by parameters 'Density' and 'SolDensity' in the 'Multiple Fitting Parameters'. It is important to note here that if either solute or solvent contains a resonant element along with other non-resonant elements the

'Density' or 'SolDensity' represents only the density of non-resonant elements. The software will calculate the overall density of the material using 'Rmoles' of the resonant element. For example, for a solution of RbCl in H_2O the material should be described as RbCl:H2O, the 'Density' should be the density of the Cl and 'SolDensity' should be the density of H2O. If the material is described by a single element including the resonant element then the 'Density' should be the density of the element itself.

The simulation of SAXS-term, Cross-term, and Anomalous-term was calculated from the parallelepiped model of CNCs using 'Parallelepiped_Uniform' function in XModFit.[3] The core-dimensions used for the CNCs are L=40Å, B=28Å, and H=2500Å. The molecular formula used for the CNC is for the cellulose, $C_6H_{10}O_5$, with mass density of 1.5 gm/cm^3. A Stern layer of thickness same as twice the ionic-radius of Rb^+ (3.32 Å) with density of 0.3 gm/cm^3 is also considered for the simulation along with the bulk concentration of 100mM (0.00854 gm/cm^3) Rb^+. The experimental ASAXS data were fitted using the same model with norm, L, B, and Stern layer density as fitting parameters.

Section S2. ASAXS data reduction using Sturhmann method

The energy-dependent electron density contrast from a system with energies very close to the X-ray absorption of one of the element (termed as the resonant element) within the system can be written as[4–9]:

$$\rho_e(\vec{r},E) = \rho_{eo}(\vec{r}) - \rho_{es} + v(\vec{r})(f'(E) + if"(E)) \qquad \text{S2}$$

Where $\rho_{eo}(\vec{r})$ is the energy-independent total electron density of the sample, and ρ_s is the electron density of solvent (in our case the solvent is water with $\rho_{es} = 0.334$ el/Å^3), whereas $v(\vec{r})$ is the number density of the resonant element only in the system. $(f'(E), f"(E))$ are the complex scattering factors of the resonant element.

Taking the fourier transform one can obtain the X-ray scattering as[4–9]:

$$\begin{aligned} I(\vec{q},E) &= \frac{N}{V} r_e^2 |\int \rho_e(\vec{r},E) e^{i\vec{q}.\vec{r}} \mathrm{d}\vec{r}|^2 \\ &= |\rho_{os}(\vec{q})|^2 + f'(E) Re[\rho_{os}(\vec{q})\rho_r^*(\vec{q}) + \rho_{os}^*(\vec{q})\rho_r(\vec{q})] \\ &\quad + \left(f'^2(E) + f"^2(E)\right)|\rho_r(\vec{q})|^2 \end{aligned} \qquad \text{S3}$$

Where, N/V is the number of scattering samples per unit volume, r_e is the classical electron radius, $\rho_{os}(\vec{q}) = \int (\rho_{eo}(\vec{r}) - \rho_{es}) e^{i\vec{q}.\vec{r}} \mathrm{d}\vec{r}$ and $\rho_r(\vec{q}) = \int v(\vec{r}) e^{i\vec{q}.\vec{r}} \mathrm{d}\vec{r}$ are complex numbers, Re denotes real part of the complex number. But for systems with centrosymmetric geometries like sphere, cylinder, ellipsoid, etc, these terms become real and isotropic in $\vec{q}$. Owing to that, the above equation can be further simplified into

$$\begin{aligned} I(q,E) &= \frac{N}{V}[\rho_{os}^2(q) + 2f'(E)\rho_{os}(q)\rho_r(q) \\ &\quad + \left(f'^2(E) + f"^2(E)\right)\rho_r^2(q)] \end{aligned} \qquad \text{S4}$$

The above equation holds good for monodisperse system of particles. In case of polydisperse system of particles the intensity needs to be averaged over the particle size distribution and equation S4 becomes

$$I(q,E) = \frac{N}{V}[\langle \rho_{os}^2(q)\rangle + 2f'(E)\langle \rho_{os}(q)\rho_r(q)\rangle + \left(f'^2(E) + f''^2(E)\right)\langle \rho_r^2\rangle] \quad \text{S5}$$

The first term in this equation is energy independent and can be termed as *SAXS-term* ($I_S = \frac{N}{V}\langle \rho_{os}^2(q)\rangle$). Whereas both the 2nd and 3rd terms have energy dependence. The 2nd term contains the *Cross-term* ($I_C = \frac{N}{V}\langle \rho_o(q)\rho_r(q)\rangle$) and has the contribution from the resonant element as well as all other atoms in the system. Whereas the 3rd term has the *Resonant-term* ($I_R = \frac{N}{V}\langle \rho_r^2(q)\rangle$) that only has a contribution from the resonant element. In general, just below the absorption edge of the resonant element the imaginary part of the scattering constant ($f''(E)$) of the resonant element does not change considerably. Hence, the above equation is basically a quadratic function of the real part of the scattering factor of the resonant element ($f'(E)$).

As per ASAXS experiments, we obtained the scattering intensity as a function of q and E, i.e. the left-hand side of eq. S5. In general, the complex scattering factors ($f'(E), f''(E)$) of the resonant element can be obtained from the online database of National Institute of Standards and Technology.[10] With the tabulated values for resonant element one can have a system of linear equations based on equation S4. By solving the linear equation one can obtain the values of I_S, I_C, and I_R, as mentioned here.[11]

The *Resonant-term* in the equation, in general, is a few orders of magnitude smaller than the other terms, and for most practical purposes the equation can be further approximated into:

$$I(q,E) \approx I_s + 2f'(E)I_C \quad \text{S6}$$

As the cross term is essentially a product of SAXS and Resontant terms, the *Resonant-term* can also be approximated from the non-zero *Cross-term* directly as:

$$I_R(q) = \langle \rho_R^2(q)\rangle = I_C^2(q)/I_S(q) \quad \text{S7}$$

Without any approximation the scattering terms (I_S, I_C, I_R) in Eq. S4 will have to satisfy a constraint using Cauchy-Schwarz inequality:

$$I_R(q) \geq I_C^2(q)/I_S(q) \quad \text{S8}$$

This in-equality provides a minimum limit for I_R when I_S and I_C are known and is the reason for the equality in Equation S8 under approximation. We applied both the constraints in S7 and S8 on the energy-dependent simulated data from the parallelepiped model as discussed in the main text to obtain the scattering terms. The data reduction process is implemented in one of the packages 'XAnoS_Components' under the software suite 'XAnoS' developed at NSF's ChemMatCARS.[12] Due to the presence of statistical variances in the data and the very weak contribution of the resonant term in the energy-dependent data, we found the equality constraint to provide resonant terms with narrow error bars.

References

(1) Macke, N.; Hemmingsen, C. M.; Rowan, S. J. The Effect of Polymer Grafting on the Mechanical Properties of PEG-Grafted Cellulose Nanocrystals in Poly(Lactic Acid). *Journal of Polymer Science* **2022**, *60* (24), 3318–3330. https://doi.org/10.1002/POL.20220127.

(2) Mao, Y.; Liu, K.; Zhan, C.; Geng, L.; Chu, B.; Hsiao, B. S. Characterization of Nanocellulose Using Small-Angle Neutron, X-Ray, and Dynamic Light Scattering Techniques. *Journal of Physical Chemistry B* **2017**, *121* (6), 1340–1351. https://doi.org/10.1021/ACS.JPCB.6B11425/SUPPL_FILE/JP6B11425_SI_001.PDF.

(3) Bera, M. K.; Bu, W. XModFit: X-Ray Modeling and Fitting. **2022**. https://doi.org/10.5281/ZENODO.7047225.

(4) Stuhrmann, H. B. Anomalous Dispersion of Small-angle Scattering of Horse-spleen Ferritin at the Iron K Absorption Edge. *Acta Crystallographica Section A* **1980**, *36* (6), 996–1001. https://doi.org/10.1107/S0567739480002033.

(5) Ballauff, M.; Jusufi, A. Anomalous Small-Angle X-Ray Scattering: Analyzing Correlations and Fluctuations in Polyelectrolytes. *Colloid Polym Sci* **2006**, *284* (11), 1303. https://doi.org/10.1007/S00396-006-1516-5.

(6) Tatchev, D. Structure Analysis of Multiphase Systems by Anomalous Small-Angle X-Ray Scattering. *https://doi.org/10.1080/14786430802279760* **2008**, *88* (12), 1751–1772. https://doi.org/10.1080/14786430802279760.

(7) Sztucki, M.; Di Cola, E.; Narayanan, T.; Sztucki, M.; Cola, E. Di; Narayanan, T. New Opportunities for Anomalous Small-Angle X-Ray Scattering to Characterize Charged Soft Matter Systems. *J Phys Conf Ser* **2011**, *272* (1), 012004. https://doi.org/10.1088/1742-6596/272/1/012004.

(8) Sztucki, M.; Di Cola, E.; Narayanan, T. Anomalous Small-Angle X-Ray Scattering from Charged Soft Matter. *The European Physical Journal Special Topics 2012 208:1* **2012**, *208* (1), 319–331. https://doi.org/10.1140/EPJST/E2012-01627-X.

(9) Wieland, D. C. F.; Schroer, M. A.; Gruzinov, A. Y.; Blanchet, C. E.; Jeffries, C. M.; Svergun, D. I. ASAXS Measurements on Ferritin and Apoferritin at the BioSAXS Beamline P12 (PETRA III, DESY). *J Appl Crystallogr* **2021**, *54* (Pt 3), 830–838. https://doi.org/10.1107/S1600576721003034.

(10) Phys Lett, A.; Chantler, C. T. Detailed Tabulation of Atomic Form Factors, Photoelectric Absorption and Scattering Cross Section, and Mass Attenuation Coefficients in the Vicinity of Absorption Edges in the Soft X-Ray (Z=30–36, Z=60–89, E=0.1 KeV–10 KeV), Addressing Convergence Issues of Earlier Work. *J Phys Chem Ref Data* **2000**, *29* (4), 597–1056. https://doi.org/10.1063/1.1321055.

(11) Sztucki, M.; Di Cola, E.; Narayanan, T. Instrumental Developments for Anomalous Small-Angle X-Ray Scattering from Soft Matter Systems. *urn:issn:0021-8898* **2010**, *43* (6), 1479–1487. https://doi.org/10.1107/S002188981003298X.

(12) Bera, M. K. XAnoS: X-Ray Anomalous Scattering. *Zonedo*. 2023.